https://doi.org/10.5194/egusphere-2026-2498
Preprint. Discussion started: 13 May 2026

Observations of the multi-year variability of mixing in shelf seas

Chris A. Whitwell[1,2], Nicole L. Jones[1], Gregory N. Ivey[1], and Matthew D. Rayson[1]

[1]School of Earth and Oceans and Oceans Institute, University of Western Australia, 35 Stirling Highway, Crawley, Perth, 6009, Australia
[2]DHI Water and Environment, 9 The Esplanade, Perth, 6000, Australia

Correspondence: Chris A. Whitwell (chris.a.whitwell@outlook.com)

Abstract. We present 5-year long continuous mixing observations from four mooring locations, spanning 10° degrees of latitude, on the continental shelf of North-Western Australia. The sites are subject to a diverse range of atmospheric and oceanic forcing and each has distinct local bathymetry. We estimated the diapycnal diffusivity and vertical turbulent heat flux at all sites and throughout the water column using a fine-scale mixing length model. There were four dominant peaks in the power spectrum: annual, spring-neap, diurnal, and semi-diurnal. We examined the variability in the mixing at all sites in terms of the seasonal stratification, depth, and tidal range and phase. The highest annual variability occurred at the highest latitude sites which had the greatest seasonal variation in stratification. The mixing also varied with the strength of the dominant tidal constituents (both baroclinic and barotropic). Heat flux was a more useful measure of mixing than diffusivity due to the strong seasonal variations in density stratification on the shelf. Finally, we provide guidance on the determination of the appropriate sampling period to adequately describe the mixing, and discuss the effects of short sampling periods on the ability to describe the long-term mixing.

1 Introduction

Diapycnal mixing in shelf seas is an important process responsible for the transport of heat, salt, nutrients, and other tracers, such as contaminants, in the presence of a density gradient. Diapycnal mixing transports nutrients upward to the well-lit surface layer in shelf seas, resulting in increased primary productivity (Huisman et al., 2006) and, due to the downward transport of heat, can play an important role in the mitigation of thermal stress events in surface waters (Wyatt et al., 2020). Compilations of field observations of diapycnal mixing(Waterhouse et al., 2014; Inall et al., 2021) indicate that observations are typically scarce over both space and time and, due to the inherent intermittency of diapycnal mixing (Portwood et al., 2016; Taylor et al., 2019), interpretation of the observations can be challenging. Our understanding of the causes of the variability of diapycnal mixing is poor. In part due to the intermittency, diapycnal mixing is not well represented in ocean models, which rely on sub-grid parameterizations to account for diapycnal mixing, and these challenges are especially important in shelf seas (Savelyev et al., 2022; Luneva et al., 2019) with their high energy forcing and large variability on time periods from subtidal to seasonal and beyond.

The evaluation and improvement of the sub-grid scale parameterizations of diapycnal mixing is the subject of ongoing research from field, numerical, and laboratory studies. Field studies have the distinct advantage of directly capturing the energetic

https://doi.org/10.5194/egusphere-2026-2498
Preprint. Discussion started: 13 May 2026

flows and complexity of both the forcing and topography in shelf seas, and can thus provide a direct measure of the performance of sub-grid closure schemes. However, historically field observations of mixing have typically been limited to relatively short deployments because of the cost- and time-intensive nature of collecting data. In order to capture low-frequency variation in diapycnal mixing, we thus require long time-series observations of diapycnal mixing. Such observations are rare (e.g., Moum, 2021; Warner and Moum, 2019) but recent work (Ivey et al., 2018; Bluteau et al., 2016; Whitwell et al., 2024) demonstrates a reliable means of collecting long-term temporal records of mixing from moorings, enabling the examination of diapycnal mixing variability at the tidal and seasonal time scales.

Winters et al. (1995) formally defined irreversible diapycnal mixing as the rate of change of the background potential energy, where the “background" is defined from an adiabatic resort of the density field. Significant efforts have been made to incorporate this definition of mixing into existing mixing models (Salehipour and Peltier, 2015). However, fully executing the Winters et al. (1995) approach is not practical for field observations due to the challenges associated with observing the instantaneous 3D density field over an appropriate spatial scale in field studies. Instead, field observations typically estimate mixing by measuring the dissipation of turbulent kinetic energy ϵ (i.e., MacKinnon et al., 2017) or the dissipation of thermal variance χ, then using models to estimate the diapycnal diffusivity K_ρ (e.g., Waterhouse et al., 2014). Less commonly, studies have estimated the vertical turbulent heat flux (or density) (i.e., Shroyer et al., 2010; Jones et al., 2020) in order to evaluate irreversible diapycnal mixing. Especially in shelf seas where the background density field is highly variable both at tidal and seasonal scales, this approach is necessary to understand the spatio-temporal variability in mixing.

Determining the appropriate temporal and spatial sampling rate of diapycnal mixing has been the subject of ongoing discussion (Ivey et al., 2008; Moum and Rippeth, 2009; Cael and Mashayek, 2021). A recent direct numerical simulation study by Taylor et al. (2019) suggested that sampling programmes that fail to capture the temporal intermittency of energetic overturns could result in significantly underestimating the average diapycnal mixing. Recent field studies in shelf-seas by Couchman et al. (2021), Whitwell et al. (2024) and Lewin et al. (2025) suggest that these relatively rare energetic mixing events, rather than the “typical" (median) mixing rates, dominate the total vertical heat flux. However, these studies spanned relatively short time periods (2 days and 1 month, respectively) and horizontal spatial scales (1.5 km and 30 km, respectively). Characterising and parameterizing diapycnal mixing at a site involves accurately measuring the mixing rate and predicting the occurrence and location over depth of the most significant or energetic mixing events. Previous work (Whitwell et al., 2024) explored the relationship between significant turbulent mixing events with the forcing flows generated by relatively short-term non-linear wave events. However, it remains unclear how low-frequency processes, such as seasonal changes in stratification or spring-neap variations in tidal forcing, that are clearly important in shelf regions, influence the occurrence and intensity of these intermittent energetic mixing events.

Our study seeks to address these issues by asking the following questions:

1. What are the low-frequency processes that influence diapycnal mixing in shelf seas?

2. Does the choice of diapycnal mixing diagnostic (diffusivity or heat flux) affect our quantitative description of mixing patterns in shelf seas?

https://doi.org/10.5194/egusphere-2026-2498
Preprint. Discussion started: 13 May 2026

3. Do short-term sampling periods capture the temporal variability in diapycnal mixing in shelf seas?

We address these questions by using five years of long-term field observations at four widely separated and diverse sites, all located on the Australian North West Shelf. We begin by describing each of the four sites (Sect. 2.1), and the corresponding mooring/instrumentation configuration for each deployment (Sect. 2.2). We then describe the methods used to characterise the highly variable forcing and density structure (Sect. 2.3) and the procedure used to estimate mixing at each site (Sect. 2.4). After characterising the dynamics (Sect. 3.1), we provide an overview of the mixing observed at each site (Sect. 3.2). We then examine the dominant time scales that control the variability of mixing (Sect. 3.3), and determine the effect of the different time scales on the overall significant mixing at each of the sites (Sect. 3.4). Finally, we discuss the implications of these findings for both the quantification of ocean mixing in field studies and for mixing parameterizations in shelf seas (Sect. 4).

2 Methods

2.1 Site Descriptions

The field observations come from four widely-separated sites on the Australian North West Shelf (NWS) that are part of Australia's Integrated Marine Observing System (IMOS) (Fig.1a). The sites extend over 10° of latitude and 16° of longitude and all mooring sites were located along the 200 m isobath. For each site, we estimated the local bottom slope (Fig.1b1-4) from 250 m resolution bathymetry data (Whiteway, 2009) as $\sqrt{(dh/dx)^2 + (dh/dy)^2}$, where h is the water depth and x and y are the longitudinal and latitudinal directions.

The Barrow Island site (BAR) is the southernmost site at 21° S, located about 100 km off the coastline of north-western Australia and 60 km east of Barrow Island. The BAR site sits on a steep shelf break (slope = 0.012) that runs near north/south and at an angle of $45°$ to the coastline located further south (Fig.1.b3). Jones et al. (2020) observed breaking internal bores that greatly enhanced mixing at a site ∼150 km north-east and inshore of the BAR site, but their site is unlikely to be indicative of mixing at the BAR site as the local topography and remote internal wave forcing are significantly different. As well as locally generated internal waves, satellite altimetry data indicates that the general region around the BAR site may also be subject to remotely generated internal waves from Lombok Strait to the north, but the extent to which this forcing reaches the BAR site is uncertain given the local complexity of the bathymetry (Gong et al., 2021).

The Rowley Shoals site (ROW) is 230 km offshore and 60 km southeast of the Rowley Shoals. While the ROW site is located 60 km northeast (along shelf) of the RS2019 field study (Whitwell et al., 2024), the 0.004 slope at the ROW site is similar to the slope at the corresponding depth at the RS2019 study (0.005). A variety of internal wave types were observed at RS2019, including mode-1, mode-2 waves, and internal bores. The ROW site is both a region of local internal tide generation and is subject to remotely generated internal tides from Lombok Strait. Gong et al. (2021) observed a variety of internal wave types, including mode-1, mode-2 waves, and internal bores at RS2019. At the 200 m isobath, ocean mixing was dominated by energetic internal wave events.

https://doi.org/10.5194/egusphere-2026-2498
Preprint. Discussion started: 13 May 2026

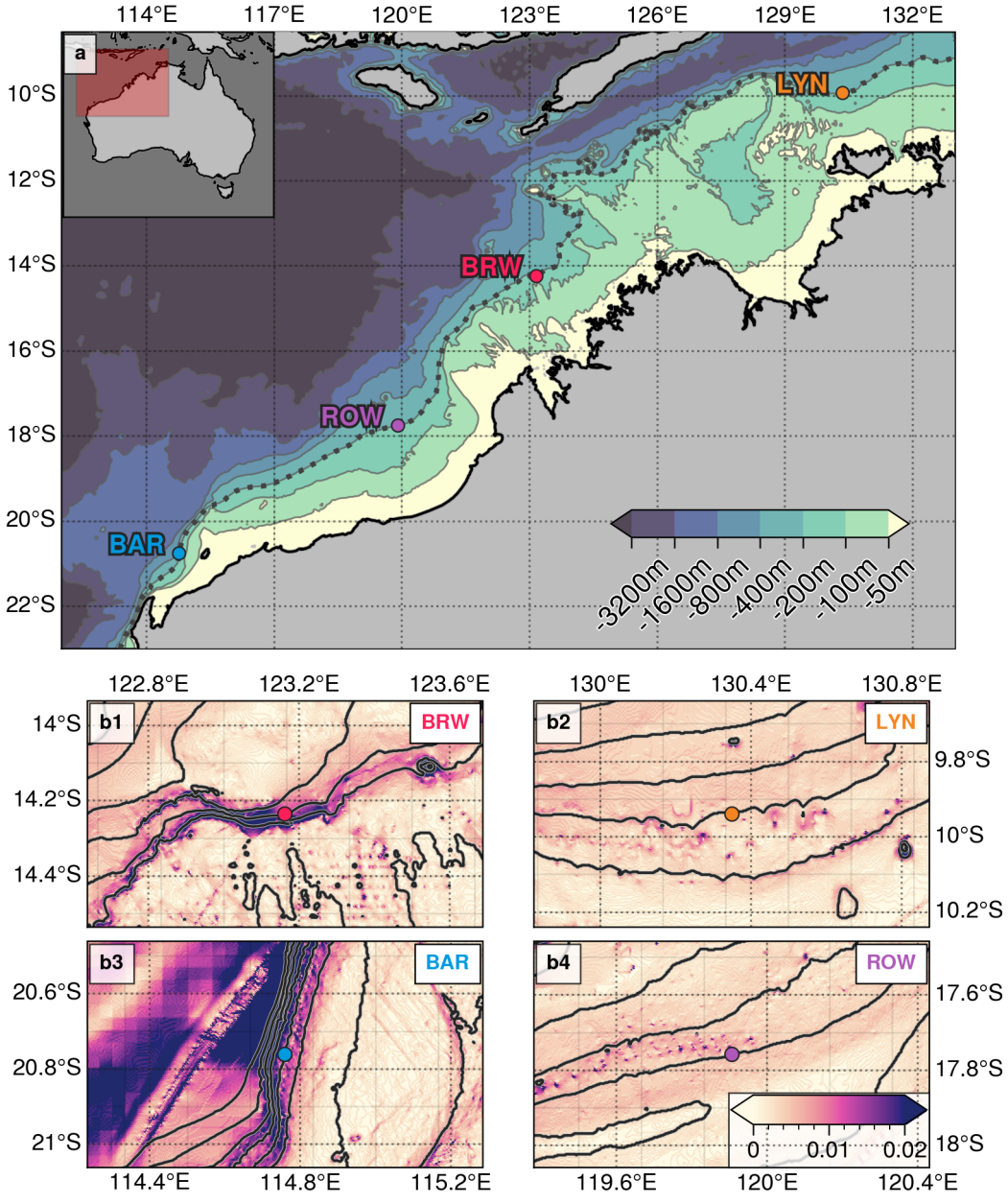

Figure 1. Panel a shows the location of each mooring used in this study. The filled contours show the bathymetry at 2.5 km resolution, and the dotted contour shows the 200 m isobath. Panels b.1-4 show the bathymetry contours for each site calculated from 250 m gridded data (every 50 m from -400 m to 0 m), and the local slope (colormap).

https://doi.org/10.5194/egusphere-2026-2498
Preprint. Discussion started: 13 May 2026

The Browse Island site (BRW) is located 200 km off the Australian coastline and 40 km west-northwest of Browse Island on a steep shelf break (slope = 0.019) on the edge of the Browse Basin. Numerical hydrostatic 3D simulations conducted by (Rayson et al., 2019) in the region show the BRW site has energetic baroclinic forcing with a strong but local offshore (north-northeastern) baroclinic energy flux. Rayson et al. (2019) (and subsequently, Zulberti et al., 2020) also observed large amplitude internal waves in the region, but these observations were made further offshore at a site with much gentler slopes (< 0.002). Similar to the ROW site, the BRW site is a region subject to both local internal tide generation as well as remotely generated internal tides (Gong et al., 2021).

Finally, the Lynedoch Shoal site (LYN) is the northernmost study site at 10° S located about 90 km east of Lynedoch Shoal and 300 km north of Darwin, and the local bottom slope was about 0.002. Unlike the other sites in this study, there is relatively little understanding of either the locally or remotely generated internal wave activity. Likewise, to our knowledge, there have been no published investigations of turbulent mixing processes near the LYN site.

2.2 Mooring Design, Deployment and Instrumentation

Each field site consisted of a single through-the-water column mooring that measured temperature, velocity, pressure, and conductivity. The number, depth, and sampling frequency of the thermistors changed between moorings and deployments over the five year observation period (Fig.2). For the analysis we only used thermistors sampling at 0.05 Hz or faster (solid blue lines in Fig. 2) to estimate fine-structure turbulent quantities. Typically there were four thermistors in the top 60 m of the water column, two thermistors at mid-depth, and three thermistors in the bottom 50 m of the water column. We included any remaining thermistors (dashed gray lines in Fig.2) when calculating background quantities (i.e. temperature/density gradients).

We obtained velocity data from co-located upward- and downward-looking moored acoustic Doppler current profilers (ADCPs, red dotted lines in Fig.2) sampling at 0.002Hz (10 minutes) with vertical bin-sizes at 8 m and 4 m from the upward- and downward-facing ADCPs, respectively. Velocity estimates were vertically bin-mapped to account for any mooring knockdown and smoothed using a 3-point rolling mean. Here we refer to “nominal" depths from an element’s along-mooring distance and the initial deployment depth, assuming a vertical mooring. Conversely, “instantaneous" depths are estimated using in-situ CTD observations. Both temperature and velocity data were filtered using the strictest quality assurance and control flags provided by IMOS. A thermistor firmware issue resulted in significant data loss from March-October 2020 at the ROW, BRW and LYN sites, while the LYN site mooring was not deployed between October 2020 and May 2021.

2.3 Site Characterization

We characterized the forcing at each site from the background stratification and the local barotropic tidal forcing. We calculated the background stratification using the buoyancy frequency N by first converting the temperature observations θ to density ρ using a linear equation of state relationship derived from CTD measurements at each site. We removed the effects of tidal displacement of the density field by using a 14-day low pass filter. We also removed estimates of N when the temperature gradient was unresolved ($d\theta/dz < 0.002$ °C/m). We characterized the barotropic forcing by using harmonic analysis to calculate the

https://doi.org/10.5194/egusphere-2026-2498
Preprint. Discussion started: 13 May 2026

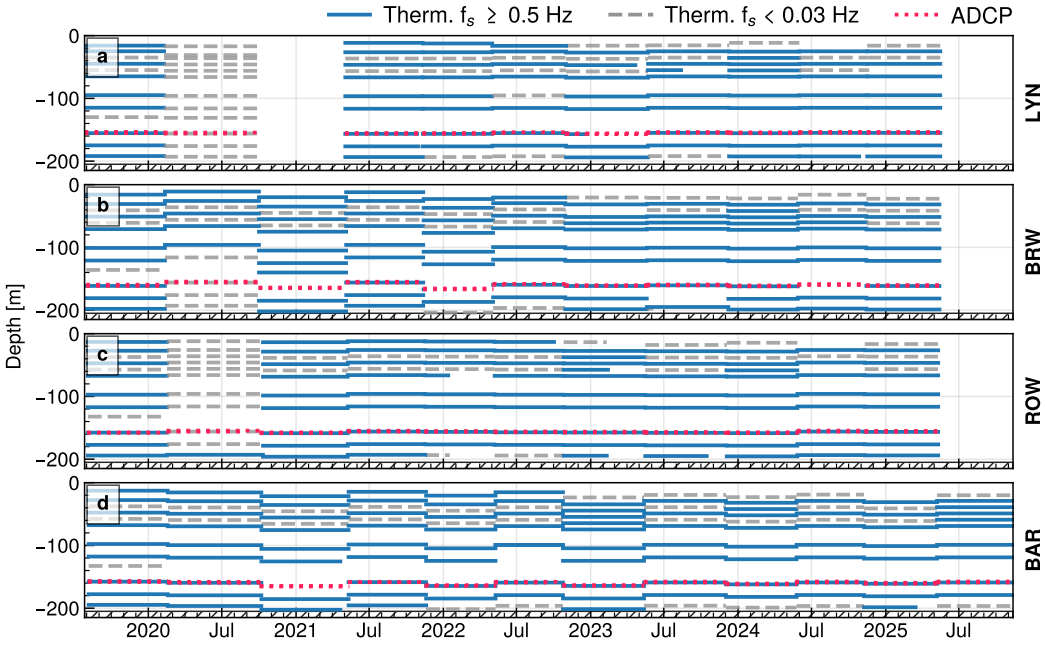

Figure 2. Panels a-d show the instrument depths for the deployments at the LYN, BRW, ROW and BAR sites, respectively. Blue solid lines show thermistors capable of measuring fine-structure turbulent quantities, gray dashed lines show thermistors suitable for background quantities, and red dotted lines indicate ADCP depths.

tidal ellipses of the three largest tidal constituents at each site. This was done by applying an 8th-order Chebyshev polynomial to 1-hour averaged velocity observations to first smooth the data, and then interpolating the result onto a uniformly spaced 10 m grid. We then depth-averaged the eastward and northward velocities to obtain the barotropic velocity and performed a tidal harmonic analysis to obtain the tidal ellipses. These measured tidal ellipses for the M_2 and S_2 constituents were compared with those predicted by the TPXO tide model from Egbert and Erofeeva (2002).

2.4 Fine-structure mixing estimates

We calculated the turbulent diapycnal diffusivity K_ρ using the fine-structure mixing length model for a shearing flow of Ivey et al. (2018). The model uses an Ellison scale, derived from the low turbulent wavenumbers , and the vertical shear S. Ivey et al. (2018) and Whitwell et al. (2024) found, from comparison with direct microstructure estimates of diffusivity, that a robust estimate of the diapycnal diffusivity is given by:

$$K_\rho = 0.09 {L_E}^2 S \tag{1}$$

where $L_E = \tilde{\theta}/(d\bar{\theta}/dz)$ is the Ellison length scale, $\tilde{\theta}$ is the root-mean-square of the turbulent temperature fluctuations θ', $d\bar{\theta}/dz$ is the background temperature gradient and the background shear $S = d\bar{\mathbf{u}}/dz$. The model assumes that both S and $d\bar{\theta}/dz$ re-

https://doi.org/10.5194/egusphere-2026-2498
Preprint. Discussion started: 13 May 2026

main constant over the vertical length scale L_E. The Ellison length scale estimate must be free of contamination from reversible internal wave field displacements. Here we followed Jones et al. (2020) and Cimatoribus et al. (2014) and used time-frequency analysis to remove any internal wave contributions when estimating L_E. We first estimated the local 20-minute minimum buoyancy period, T_{BP-min}, from the 30-minute low pass filter of the density estimates from Sect. 2.3 to determine the shortest time scale affected by internal waves. We then used a maximal overlap discrete wavelet transform (MODWT) (Percival and Walden, 2000) with a least-asymmetric mother wavelet (length 8) to perform a scale-based decomposition of the temperature variance, which we then integrated over all time-scales shorter than T_{BP-min} to estimate $\tilde{\theta}$. Finally, we reconstructed the background (non-turbulent) temperature field by performing an inverse MODWT on the wavelet and scaling coefficients associated with time scales longer than T_{BP-min} to calculate $d\bar{\theta}/dz$. The method performs poorly when the stratification is very weak, so we removed any estimates when $d\bar{\theta}/dz < 0.001°$C/m, and for very weak shear, so we removed any estimates when $S < 0.004\text{s}^{-1}$. We also performed hard thresholding on the wavelet coefficients using the universal threshold (Percival and Walden, 2000) to remove the effects of instrument noise ($\sigma_\varepsilon = 0.001°\text{C}$) on the estimates of $\tilde{\theta}$.

To account for the potential effects of the short-term, non-turbulent straining of the local density field due to the background baroclinic tidal motions, we also calculated the vertical turbulent heat flux

$$\text{J}_\text{Q} = \bar{\rho} C_p K_\rho (d\bar{\theta}/dz) \tag{2}$$

where $\bar{\rho}$ is the average density, C_p is the heat capacity of water, and K_ρ is estimated from equation 1. As heat flux $\text{J}_\text{Q} \propto (d\theta/dz)^{-1}$, it has a weaker dependence on the accuracy of the estimation of the temperature gradient than K_ρ, an effect that can become important during periods of strong internal wave straining when the density gradient locally weakens.

3 Results

Using the methods discussed in Sect. 2, we begin with characterization of the dynamics at each site, followed by an overview of mixing observations over the entire record. We then examine the dominant frequencies controlling mixing, and finally determine the contribution of each dominant frequency to the total observed mixing.

3.1 Site Characterization

The background stratification varied seasonally at all sites (Fig.3). From November to early May (late spring to late autumn in the southern hemisphere), we typically observed the strongest stratification near the surface (upper 50 m), with the underlying water column remaining stratified until very near the seabed. From May to early October (late autumn to late spring), we typically observed weak stratification in the upper region of the water column and the maximum stratification near the seabed (below 150 m). The weakly stratified surface layer was particularly deep at the most southerly BAR site, extending to depths of 150 m in winter (Fig.3 a).

The stratification at the most northerly LYN site was significantly different from the other sites (Fig.3 a). Whilst strong near-surface stratification was present during summer, we also observed significant near-bed stratification over the same period.

https://doi.org/10.5194/egusphere-2026-2498
Preprint. Discussion started: 13 May 2026

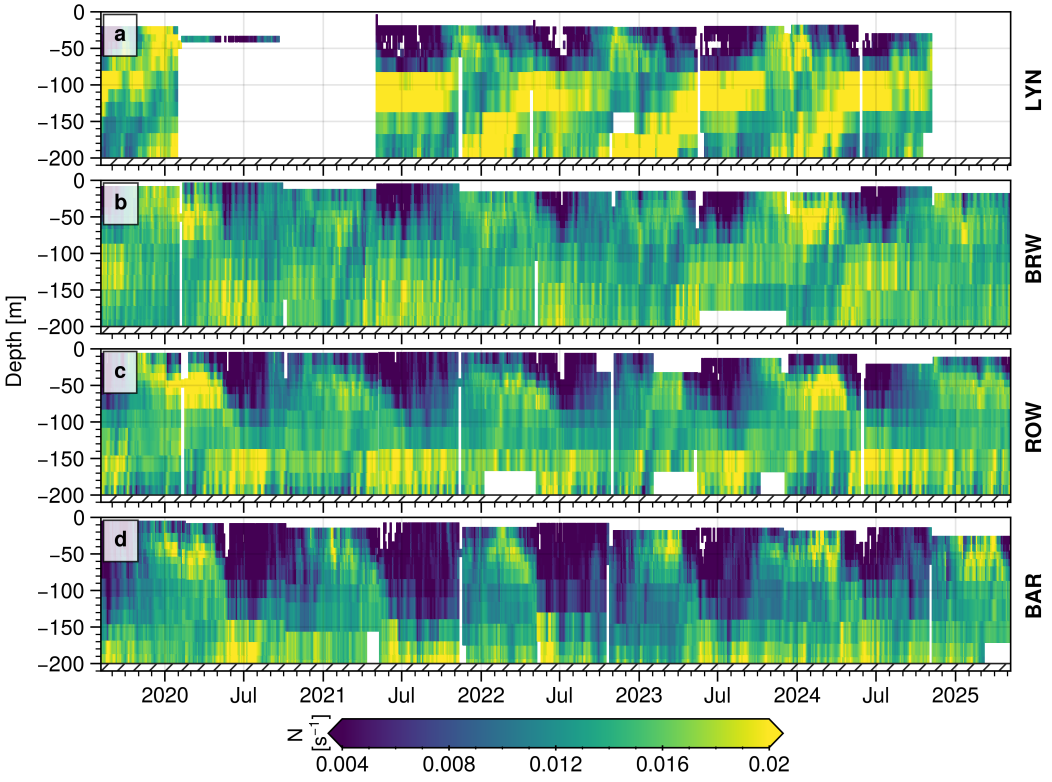

Figure 3. 14-day low pass stratification for each site. We removed estimates of N when the background temperature gradient was unresolved ($d\theta/dz < 0.002^{\circ}\mathrm{Cm}^{-1}$).

While the top half of the water column was weakly stratified during the winter months, the stratification was strongest at mid-depth, with a significant decrease in stratification nearer the bed.

The barotropic tidal forcing varied greatly in both magnitude and direction between the four sites (Fig. 4). The M_2 barotropic tide was the dominant tidal constituent at all sites, and the three most energetic frequencies (M_2, S_2, and K_2) accounted for 71%, 95%, 94% and 68% of the total barotropic tidal energy at BAR, ROW, BRW, and LYN, respectively. The tidal ellipses' major axis were oriented across the shelf at ROW, BRW, and LYN, but along the shelf at BAR. There was a significant S_2 tidal component (and hence spring-neap variability) at the two southerly sites (i.e. ROW and BRW). The barotropic tide was most energetic at the ROW and BRW sites, where the predicted M_2 tidal amplitudes were both 1.5 m, while at the southerly BAR and northerly LYN sites, the M_2 tidal amplitudes were 0.6 and 0.75 m, respectively. The observed tidal velocities for the M_2 and S_2 tides were in good agreement with those predicted using the TPXO tide model, especially at the BAR, ROW and LYN sites. At the BRW site, the magnitude of the major axis of the observed tides was 20% smaller than those predicted by TPXO. The relatively low barotropic tidal energy at BAR and LYN suggests that at these sites wind forcing may also influence the observed local ocean currents.

https://doi.org/10.5194/egusphere-2026-2498
Preprint. Discussion started: 13 May 2026

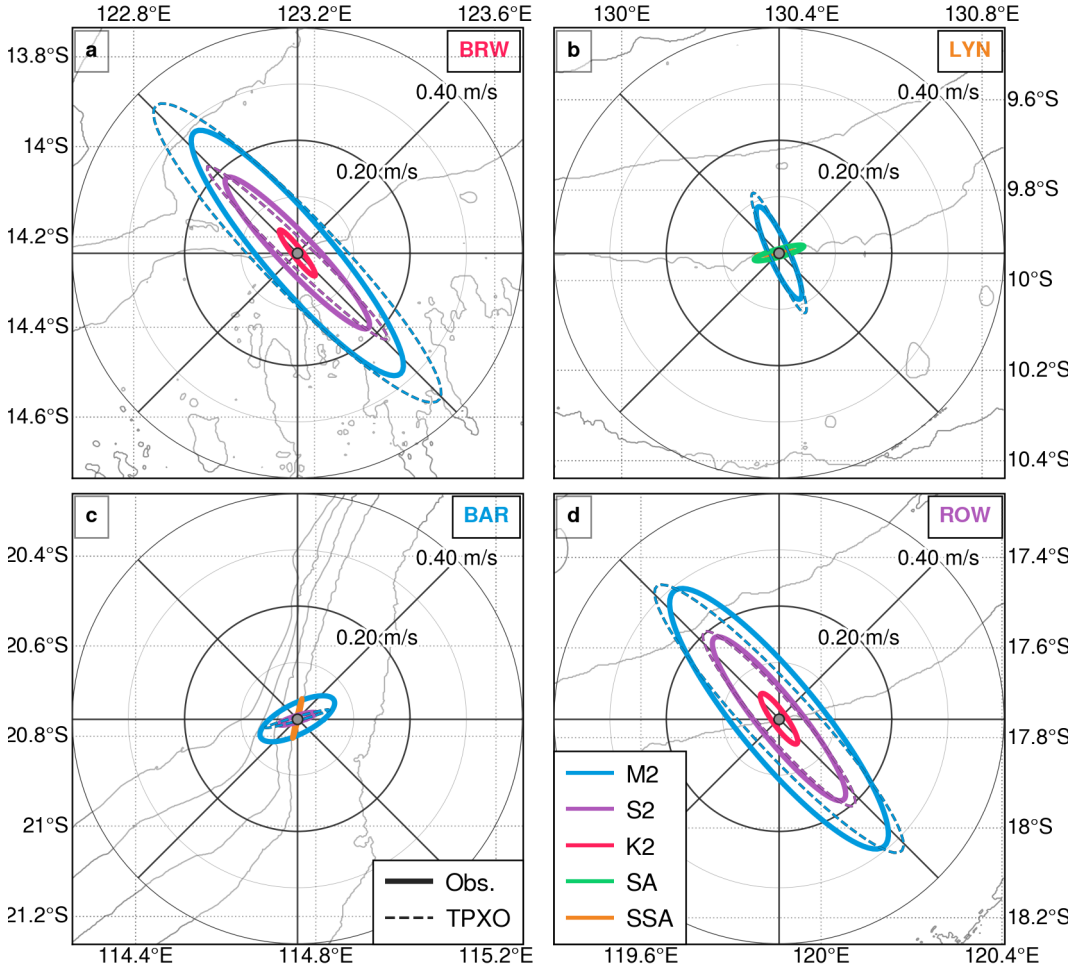

Figure 4. Panels a-d show the observed barotropic tidal velocity ellipses for the three largest tidal constituents by amplitude calculated from harmonic analysis at the BRW, LYN, BAR, and ROW sites, respectively. The resulting constituents were the principal lunar and solar semidiurnal (M_2 and S_2), the lunisolar semi-diurnal (K_2), the solar annual (SA), and the solar semiannual (SSA). Dashed ellipses show the tidal predictions obtained from TPXO for comparison.

https://doi.org/10.5194/egusphere-2026-2498
Preprint. Discussion started: 13 May 2026

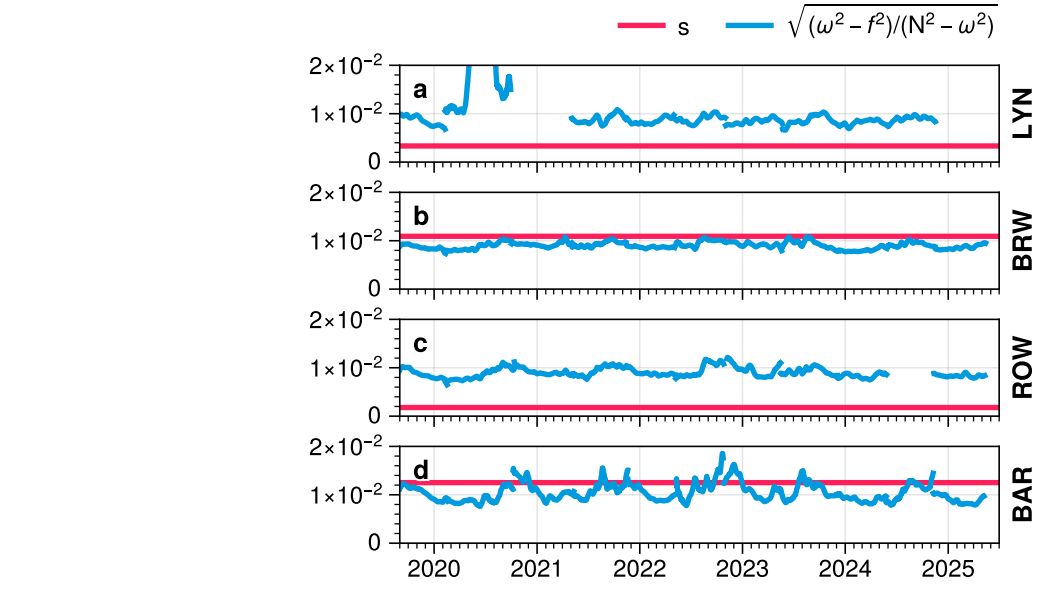

Figure 5. Topographic slope in the direction of major barotropic M_2 tidal axis s (red) and M_2 internal tide beam slope (blue) for each site.

We estimated the criticality of the local topography by comparing the slope of the M_2 internal tide beams $\sqrt{\frac{\omega^2 - f^2}{N^2 - \omega^2}}$, where f is the Coriolis parameter, ω is the angular frequency of the M_2 tide, and N the depth average 14-day low pass stratification, to the topographic slope s in the direction of the major axis of the M_2 barotropic tidal ellipse (Fig.5). The LYN and ROW sites, which had much gentler slopes (Fig. 1 b.2 & 4), remained subcritical throughout the entire record. The BRW site (Fig. 1 b.1) was typically supercritical but did become (near-)critical during August and September each year. The slope was also typically supercritical at the BAR site. However, the highly variable stratification at this site (Fig. 3 d) resulted in the slope becoming sub-critical from August-October each year.

3.2 Overview of mixing statistics

As noted by Scheifele et al. (2021), the use of medians and means or averages for turbulent quantities and mixing observations can have distinctly different interpretations. For each site and, using the nearest sensor observations within 10 m, for each nominal depth at 25 m intervals we produced time series of mixing. From these time series, we then calculated the record median and mean for both the diffusivity and the vertical heat flux at discrete depth intervals for each site.

The record average diffusivity $\bar{K}_\rho$ was more than a decade larger than the median at all depths and at all sites (Figure 6 column a). Despite differences in the stratification (Fig.3) and the strength of the barotropic forcing (Fig.4), $\bar{K}_\rho \sim 10^{-3}\mathrm{m}^2\mathrm{s}^{-1}$ at all sites and over depth. At the BAR and LYN sites, $\bar{K}_\rho$ was largest near the surface and decreased towards the bed. Conversely, $\bar{K}_\rho$ at ROW and BRW was larger at the top and bottom of the water column, with the minima at mid-depth. The variability of $\bar{K}_\rho$ with depth was 0.4 of a decade at BAR (Fig.6 a1) and a decade at LYN (Fig.6 a4).

https://doi.org/10.5194/egusphere-2026-2498
Preprint. Discussion started: 13 May 2026

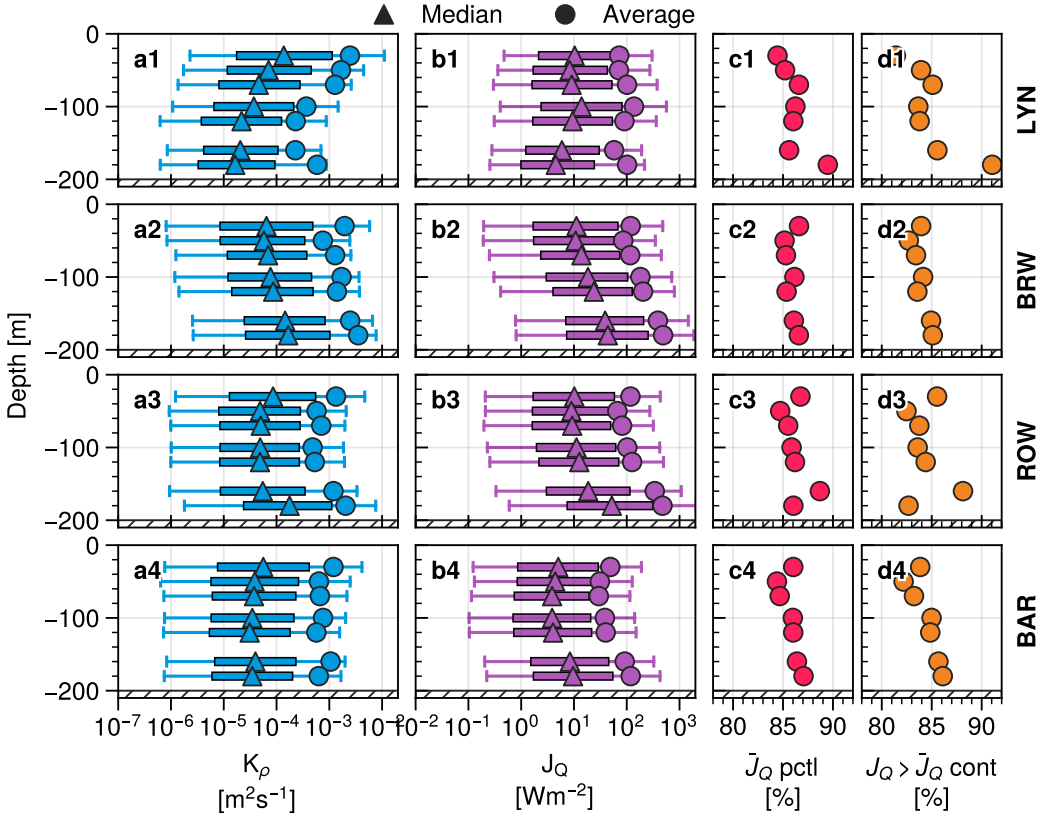

Figure 6. Mixing estimates at nominal depths for each site (rows 1-4) for the entire record. Columns a and b show the median (triangles) and mean (circles) diffusivity (blue) and vertical turbulent heat flux (purple), respectively. The horizontal box and whisker plots denote the interquartile range and the 5th-95th percentiles. Column c shows the percentile of $\bar{J}_Q$, and column d shows the percent contribution to the total heat flux from observations larger than $\bar{J}_Q$.

Like diffusivity the record average vertical heat flux $\bar{J}_Q$ was a decade larger than the median at all depths and at all sites (Figure 6 column b). The profiles of $\bar{J}_Q$ (Fig. 6 column b) indicate that ROW and BRW were more active sites for mixing than BAR and LYN. The $\bar{J}_Q$ vertical profiles were significantly different to those of $\bar{K}_\rho$ due to the effect of the vertically variable stratification. The BAR, ROW and BRW sites all showed $\bar{J}_Q$ increasing towards the bed, with the difference between the top and bottom $\bar{J}_Q$ values reaching as large as a decade. This occurred despite the large $\bar{K}_\rho$ near the surface at all sites. The LYN site differed from the others with the maxima of $\bar{J}_Q$ at mid-depth, where the stratification was, on-average, larger than at the top of the water column where $\bar{K}_\rho$ was on-average largest.

The observed near-bed enhancement of both $\bar{K}_\rho$ and $\bar{J}_Q$ at the ROW site was consistent with nearby observations by Whitwell et al. (2024) who showed the near-bed enhancement of mixing was driven by localised near-bottom internal bore

https://doi.org/10.5194/egusphere-2026-2498
Preprint. Discussion started: 13 May 2026

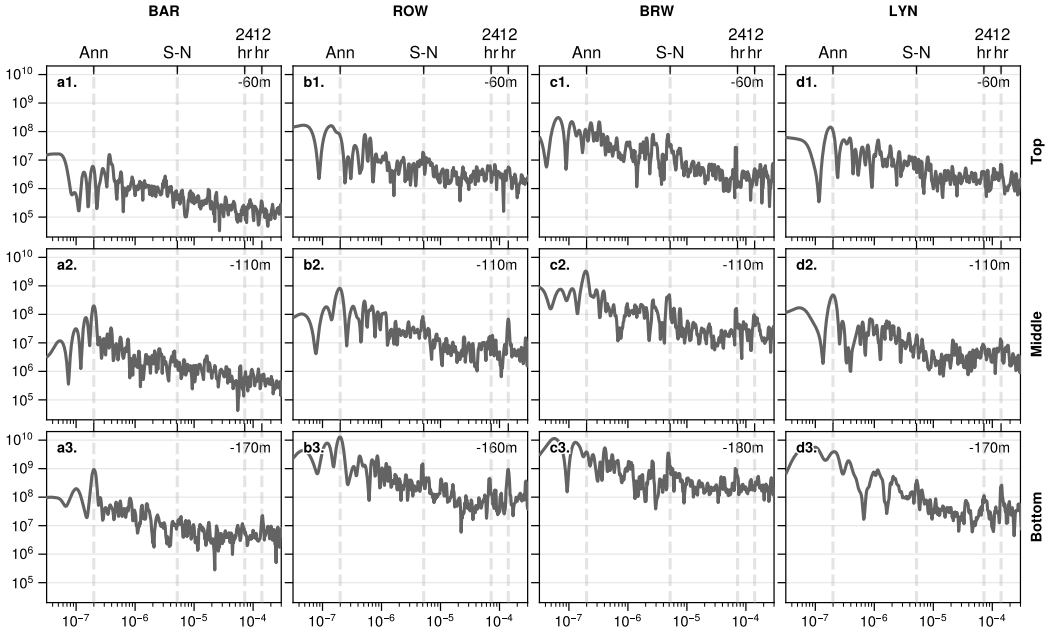

Figure 7. Spectra of 3-hour averaged J_Q at nominal depths for each site (columns a-d). Vertical dashed lines show the annual (365 days, Ann), spring-neap (S-N), 24-hour (24hr) and 12-hour (12hr) periods

activity. It remains unclear which mechanisms were driving the near-bed enhancement of $\bar{K}_\rho$ and $\bar{J}_Q$ at the BAR and BRW sites.

The mean vertical heat flux $\bar{J}_Q$ occurred around the ~85th percentile of all estimates (Fig. 6 column c). The 15% of events which had $J_Q > \bar{J}_Q$ account for 85% of the total heat flux (Fig. 6 column d). Relatively rare but energetic mixing events thus dominated the total mixing at all sites, consistent with the results from the relatively short month-long study at one site by Whitwell et al. (2024), and is consistent with ship based microstructure observations presented in Lewin et al. (2025).

3.3 Temporal variability of mixing

To quantify the long-term variability of mixing, we analyzed the vertical turbulent heat flux spectra from representative depths in the upper, mid, and lower regions of the water column. The nominal depths were chosen for each site by using the most continuous time series possible to perform the analysis. With our focus on low frequency variability, for each depth we calculated the spectra using 3-hour averaged J_Q estimates using Lomb-Scargle's (Lomb, 1976; Scargle, 1982) method for unevenly spaced time series.

The resultant vertical turbulent heat flux spectra (Fig. 7) varied greatly both between sites and with depth. The spectral energy levels typically increased with depth - except for the LYN site where the surface was the most energetic, likely due to the stronger influence of wind as discussed above. The spectral energy levels at the relatively weak tidally-forced BAR site

https://doi.org/10.5194/egusphere-2026-2498
Preprint. Discussion started: 13 May 2026

were about an order of magnitude lower than at the other sites, for comparable depths. All sites show peaks at the annual frequency. At the ROW and BRW sites, there were also notable peaks at the spring-neap period (14 days) associated with the known energetic semi-diurnal (M_2 and S_2)(Fig.4 a and d) and diurnal (O_1 and K_1) tidal constituents. A peak at the spring-neap period was not observed at any depths at the BAR and LYN sites (and was also weak near the surface at ROW). We observed peaks at the semi-diurnal frequency at all sites, especially at the mid- and lower-nominal depths. The relative magnitudes of these semi-diurnal peaks reflected the observed magnitudes of the M_2 and S_2 tidal velocities at each site (Fig.4).

The results suggest that mixing on the shelf is thus influenced by up to four dominant frequencies: seasonal, spring-neap, diurnal and semi-diurnal. In the next section we examine the variability of both K_ρ and J_Q at these four frequencies/time scales.

3.3.1 Seasonal variability of mixing

To account for the significant seasonal changes in the stratification at all sites, we divided each 5-year long record into 6-monthly “summer" periods (1st November - 1st May) and 6-monthly “winter" periods (1st May - 1st November) and applied a 14-day low pass filter to remove the tidal signals. While there are transitional periods between the summer and winter periods, with much more vertically uniform stratification, these periods were typically short. The nominal summer and winter seasons differ from the formal season definitions used in the southern hemisphere, but they are very similar to the tropical wet and dry seasons observed in northern Australia. Typically, the summer periods are characterized by a near-surface thermocline with stratification present down to near the seabed, whilst the winter periods show a mixed or weakly stratified upper water column and much stronger stratification towards the seabed.

As a consequence of the weaker stratification in winter, the average K_ρ was larger during winter (Fig. 8 b). The largest diffusivity was almost always at the surface and, during winter, values approached $10^{-2}\ m^2 s$. The greatest seasonal changes in K_ρ were observed at the BAR site, with winter values about a decade higher than summer values over the whole water column (Fig. 8 b.4). The BRW, ROW, and BAR sites all showed near-bed enhancement of diffusivity 8 b.2, 3, 4). This near-bed intensification was particularly strong at the BRW site during summer (Fig.3b.2), when the near-bed diffusivity exceeded the surface diffusivity.

As with K_ρ, the vertical heat flux J_Q was typically larger during winter (Fig. 8c). The seasonal variability was much smaller, however, reflecting the weaker dependence on the stratification. In both summer and winter, and unlike the surface-intensified K_ρ, heat flux J_Q typically increased towards the bed. Regions where both diffusivity and stratification were large, such as approaching the bed at BRW and ROW, had particularly large values of J_Q near $10^3\ Wm^{-2}$.

3.3.2 Spring-neap cycle variability of mixing

We examined the spring-neap variability by using the results of the harmonic analysis from Sect. 3.1 to reconstruct the M_2 and S_2 surface tide velocities in the direction of the tidal ellipses’ major axis, and used a Hilbert transform to calculate the envelope/amplitude of the tidal velocity time series. We then defined “spring" periods as those where the amplitude of the tidal velocity was greater than the record median, while “neap" periods were those with amplitudes less than the record median. This

https://doi.org/10.5194/egusphere-2026-2498
Preprint. Discussion started: 13 May 2026

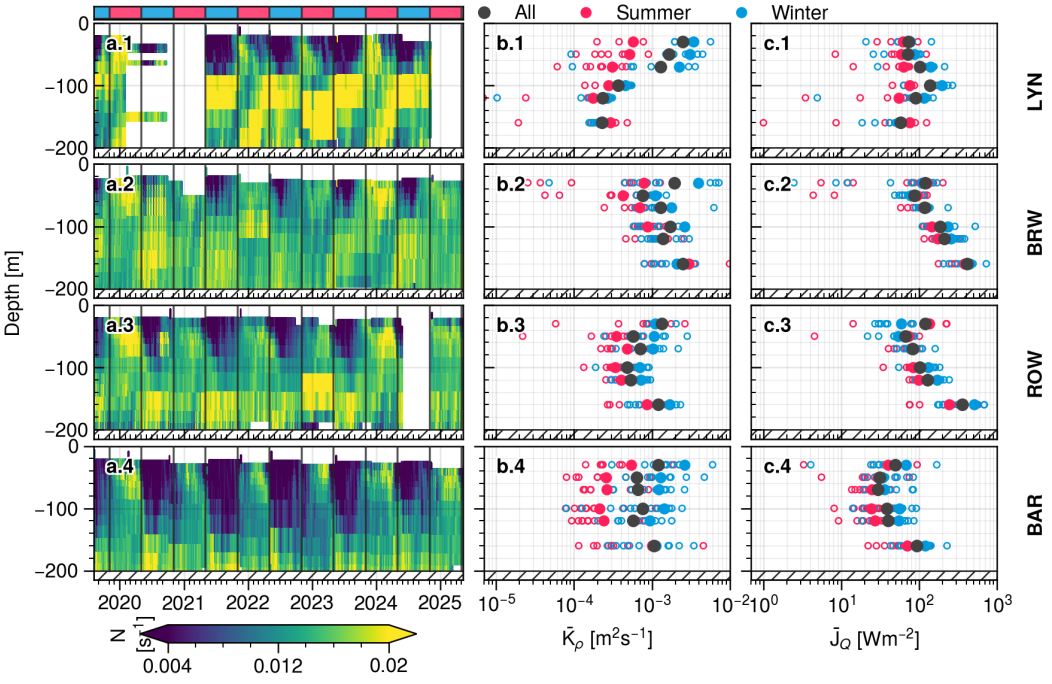

Figure 8. Columns a, b and c show the 14-day low-pass stratification, time-averaged diffusivity $\bar{K}_\rho$ and time-averaged vertical turbulent heat flux $\bar{J}_Q$. Rows 1-4 show observations from LYN, BRW, ROW and BAR sites, respectively. The gray dots indicate time-averages over the whole study, whilst the red and blue dots show the time-average over the summer and winter conditions indicated at the top of column a. Hollow markers show the averages of each individual “summer" (red) and “winter" (blue) period.

resulted in an equal distribution of observations between the spring and neap periods. We note that due to non-local generation the internal tide is not in phase with the surface tide at these sites (Rayson et al., 2021).

As both LYN and BAR have very weak S_2 forcing (Fig.4), there was little spring-neap variability at either site (Fig.9 1&4). However, both BRW and ROW have strong M_2 and S_2 tidal forcing and spring-neap variability was evident in both K_ρ and J_Q (Fig.9 2&3). Mean K_ρ and J_Q were enhanced during the spring tides, with the variability increasing towards the bed. While the magnitude of both the M_2 and S_2 tides were similar at the two sites (Fig.4 a and d), the spring-neap variability was much larger at the BRW site than at the ROW site, possibly a consequence of differing baroclinic dynamics between the sites. At the ROW site, for both spring and neap tides the diffusivity was greatest near the bed (the bottom ∼50 m) and at the surface (Fig.9 a.3), but the heat fluxes increased towards the sea bed (Fig.9 b.3). At the BRW site, for both spring and neap tides the diffusivity showed no trends with depth (Fig.9 a.2). But, similar to ROW, for both spring and neap tides the heat flux increased with depth at BRW (Fig.9 b.2).

https://doi.org/10.5194/egusphere-2026-2498
Preprint. Discussion started: 13 May 2026

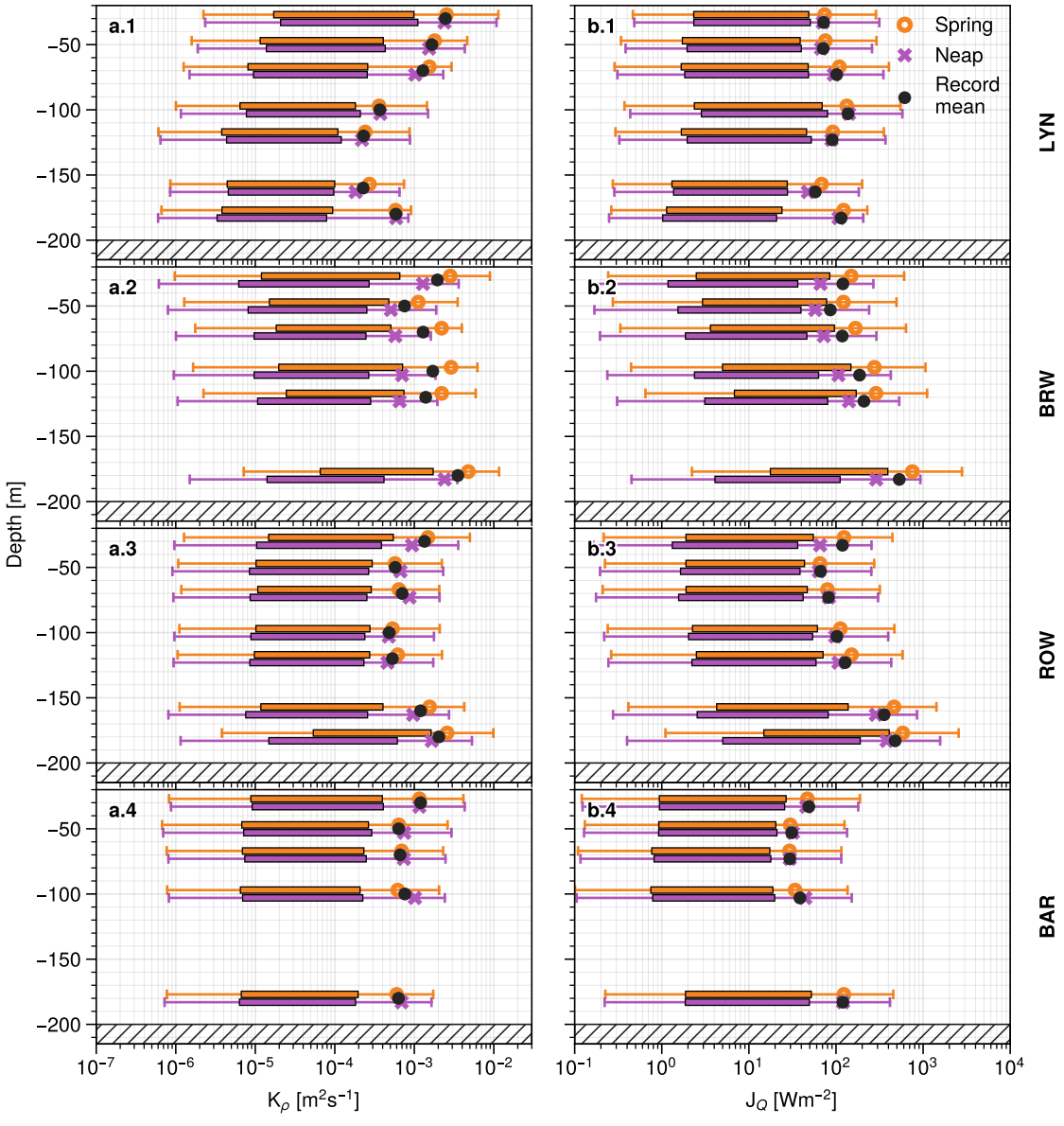

Figure 9. Diffusivity K_ρ (column a) and vertical turbulent heat flux J_Q (column b) averaged over spring tides (orange circles) and neap tides (purple crosses) for nominal depths at each site (rows 1-4). The horizontal box and whisker plots denote the interquartile range and the 5th-95th percentiles. The solid black dots show the average over the entire record, as first shown in Fig 6.

https://doi.org/10.5194/egusphere-2026-2498
Preprint. Discussion started: 13 May 2026

3.3.3 Tidal period variability of mixing

We examined the tidal variability of the mixing intensity by computing the diffusivity and heat flux at the nominal depths for both the “flood" and “ebb" phases of the dominant semi-diurnal barotropic tides. We determined the “flood" and “ebb" periods using the reconstructed M_2, S_2, and K_2 tidal velocities from Sect. 3.3.2, defining “flood" periods as when the velocity was on-shore, and “ebb" periods as when the velocity was offshore. Note that since the major axis of the tidal ellipse at Barrow Island was not cross-shore, flood tides were defined as those upslope (i.e. approximately east-north-east).

The BAR site showed little variation in either mean K_ρ or J_Q between the flood and ebb periods (Fig.10 row 4). Whilst there was an observed peak in the J_Q spectra near the bed at the BAR site (Fig. 7 a3.), we did not observe a significant enhancement of either average K_ρ or J_Q during either the flood or ebb periods, indicating that some process out of phase with the M_2 barotropic tide, such as the M_2 internal tide, influences mixing at that depth. However, the other three sites showed enhanced mixing in either the flood or ebb phase of the barotropic tide.

The ROW site, where the M_2 and S_2 barotropic tidal velocities were large (Fig.4), showed enhanced K_ρ and particularly enhanced J_Q during the flood phase (Fig.10 row 3): near the bed, the average J_Q was 5 times larger during the flood period than the ebb period. The profiles of average K_ρ or J_Q were consistent with the record averages, except for J_Q which increased dramatically near the bed during the ebb phase.

Conversely, the BRW site showed larger average K_ρ and J_Q during the ebb phase of the barotropic tide (Fig.10 row 2); likely the result of strong local offshore baroclinic energy flux at this site (Rayson et al., 2019). During the flood phase, the profile of average diffusivity did not follow the record average profile, instead showing a similar pattern to the diffusivity during neap tides (Fig.9 a.3) with a minimum at mid-depth and increasing towards both the surface and the seabed.

The LYN site, which had comparable barotropic tidal current speeds to BAR, showed enhancement of both K_ρ and J_Q during the flood tides (Fig.10 row 1). The flood and ebb tidal phases did not alter the shape of the vertical K_ρ and J_Q profiles.

3.4 Significant contributions to mixing

To examine the cumulative effect of this complex seasonal, spring-neap and tidal variability, at each site we calculated the total heat flux contribution for three nominal depths: surface, mid-level and bottom. We ensured that the record was relatively continuous and contained an equal number of seasonal, spring-neap and tidal cycles at each site (i.e., each site had the max number of summer and winter periods available given they were continuous and equal in number). This resulted in different periods over the 5-year record being used at each site due to the changing data return at each site. The resultant records did, however, cover all eight possible combinations of the dominant forcing periods (e.g. flood phase of spring tides during winter), and they each accounted for 12.5% of the total record. The resulting relative contributions to the total heat flux from the different low-frequency processes varied greatly over both the selected nominal depths and over the four field sites (Fig.11).

At the southern BAR site the variations in flux were dominated by the seasonal periodicity. Near the surface, there were no preferential periods for significant mixing (Fig.11 row 4). However, for the mid-level and bottom depths the winter periods accounted for $\sim 70\%$ of the total observed mixing (Fig.11 b.4).

https://doi.org/10.5194/egusphere-2026-2498
Preprint. Discussion started: 13 May 2026

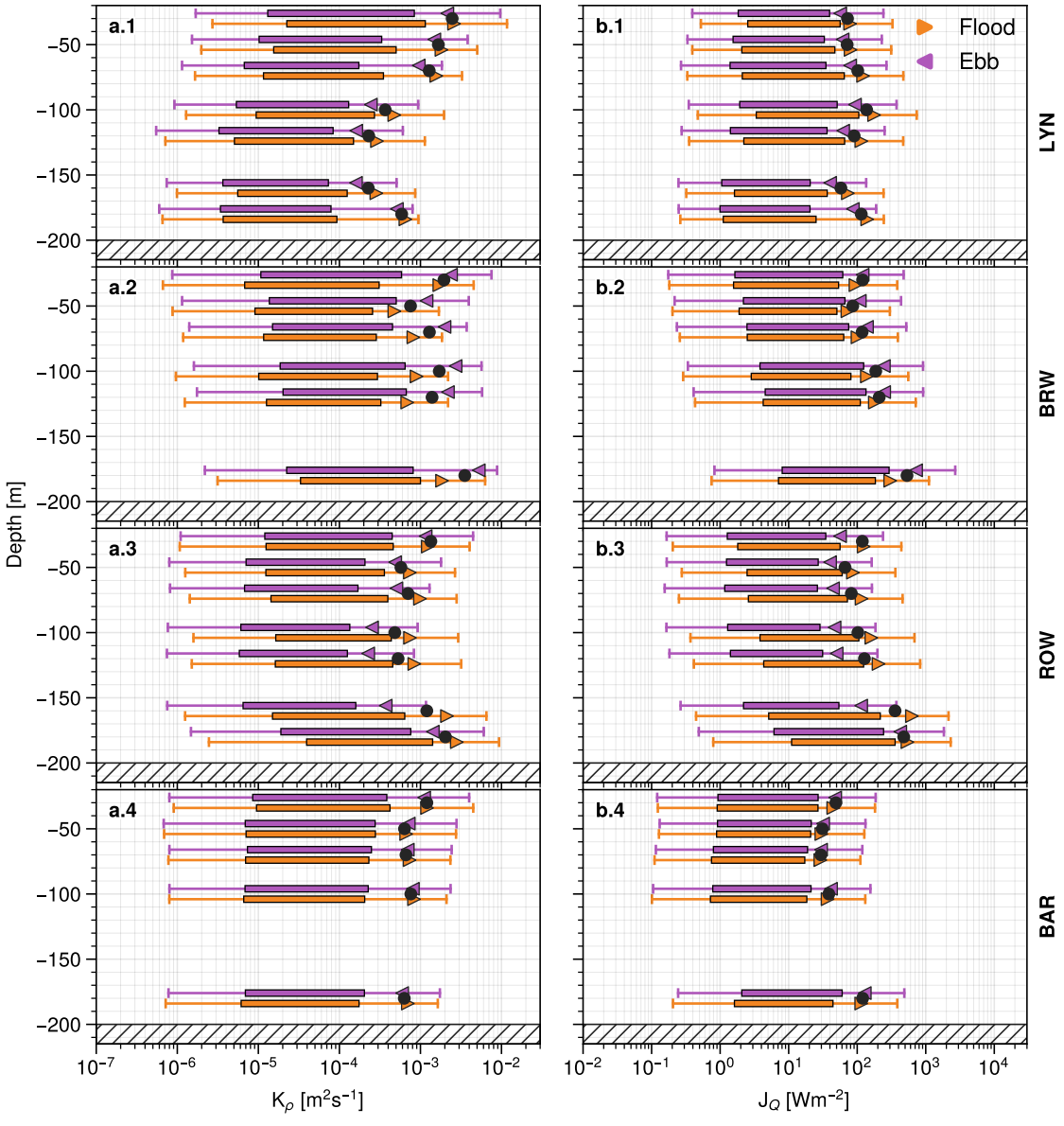

Figure 10. Diffusivity K_ρ (column a) and vertical turbulent heat flux J_Q (column b) averaged over the flood (orange right triangles) and ebb (purple left triangles) phase of the semi-diurnal tides for nominal depths at each site (rows 1-4). The solid black dots show the average over the entire record, as first shown in Fig 6..

https://doi.org/10.5194/egusphere-2026-2498
Preprint. Discussion started: 13 May 2026

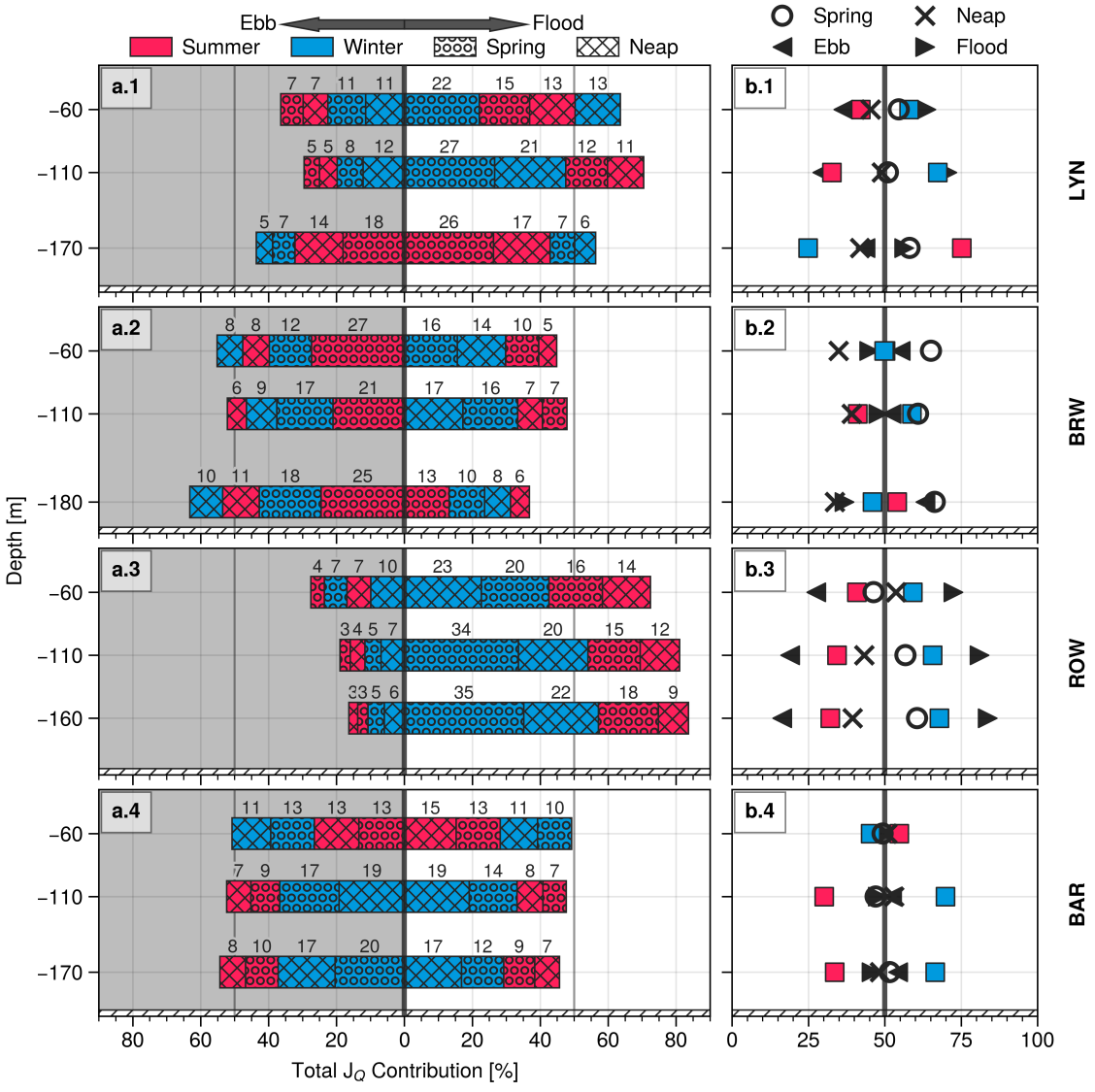

Figure 11. The contribution of different seasonal, spring-neap and tidal phases at each site (rows 1-4) to the total observed flux for three nominal depths. In column a, the colour of each bar indicates the season (red for summer and blue for winter), and the hatch of the bar indicates the spring-neap phase (circles and crosses). The white and gray regions indicate the contribution during the flood and ebb phases. The bars are descending-ordered from 0 according to their flux contribution. The numbers above each bar indicate the percent contribution to the total mixing over the time period. Column b shows the percent contribution to the total flux for each season (coloured squares), spring-neap periods (circles and crosses), and the flood-ebb periods (right and left triangles).

https://doi.org/10.5194/egusphere-2026-2498
Preprint. Discussion started: 13 May 2026

At the ROW site seasonal, spring-neap, and tidal periodicity all playing significant roles (Fig.11 row 3). In particular, the mixing was dominated by contributions during flood tides, accounting for $\sim 70-85\%$ of the total, and winter periods accounting for $\sim 60-70\%$ of the total (Fig.11 b.3). Neap tides had slightly larger contributions near the surface ($\sim 55\%$), while spring tides became increasingly important towards the bed (Fig.11 b.3).

At the BRW site there was some depth variability in the relative contributions to the total flux (Fig.11 row 2). At the upper and mid depths, spring tides and winter periods dominated the mixing, while at the bottom both spring and ebb tides and the summer tended to dominate (Fig.11 b.2). The difference in seasonal contributions decreased at the bottom where the changes in stratification between the seasons was much smaller. In contrast to the ROW site, there was a slight bias towards ebb tides, especially near the bottom, where they accounted for $\sim 60\%$ of the total heat flux (Fig.11 b.2).

As the northern LYN site has only weak spring-neap forcing, seasonal and tidal variability were the most significant (Fig.11 row 1). At the upper and mid depths, the winter period and flood tides contributed most of the mixing. Near the bed, however, the summer period dominated the variability and accounted for $\sim 75\%$ of the total observed flux (Fig.11 b.1).

3.5 Effect of record length

We investigated the effect of variations in record length by systematically partitioning the full record into shorter segments. We calculated averages of J_Q for three non-overlapping periods: 6 hours, 7 days, and 28 days. The 6-hour window was chosen so that none of the low-frequency processes discussed above were resolved, the 7-day window resolved any semi-diurnal periodicity, and the 28-day window resolved both the semi-diurnal and the spring-neap periodicity. Our record length was not sufficient to account for changes in seasonal or longer periodicity. We calculated the median, the interquartile range and the 5th and 95th percentiles of the resulting averaged J_Q, and compared them with the full record average J_Q.

The 6-hour window failed to resolve the semi-diurnal variability in J_Q. In particular, there was a range of approximately 2 decades between the 5th/95th percentiles of J_Q. Similarly, the interquartile range spans 1 decade of J_Q. The 6-hour window also failed to sufficiently capture the intermittent energetic mixing events, resulting in the median 6-hour average J_Q underestimating the long-term record averages by half a decade at all sites.

The 7-day averaging window improved this estimation of the long-term $J_Q$average at all sites, a consequence of the semi-diurnal variability of J_Q now being well resolved. The deviation of the 7-day averaged J_Q from the long-term average reduced to about 1 decade for 90% of the 7-day average estimates, with 50% of estimates of the average J_Q falling within 0.5 of a decade. Unlike the 6-hour average J_Q, the median of the 7-day window was comparable to the record average for all sites, suggesting that a 7-day record length was long enough to resolve the intermittent energetic mixing events that dominate the record average J_Q. The improvements in characterizing the long-term average J_Q were largest at the ROW and LYN sites, which showed the most significant flood-ebb tidal variability (Fig.11 rows 2 and 4).

The 28-day averaging window yielded a good estimate of the long-term average of J_Q. The deviation from the long-term average was also reduced, and 90% of estimates fell within approximately half a decade of the long-term average J_Q, and 50% of estimates fell within a factor of 2-4 of the long-term $J_Q$depending on the site. The BAR and LYN sites, which showed the strongest seasonal variability but relatively insignificant spring-neap variability, had the smallest improvements in character-

https://doi.org/10.5194/egusphere-2026-2498
Preprint. Discussion started: 13 May 2026

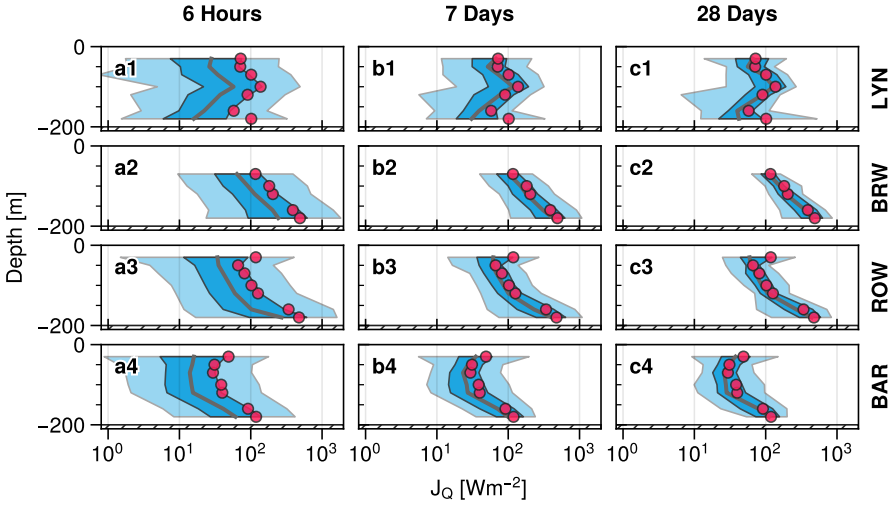

Figure 12. Effect of short record lengths on estimates of the average J_Q. For reference, the red markers show the average J_Q for the entire deployment. The dark grey lines show the median J_Q arising from record lengths of 6-hours (column a), 7-days (column b), and 28-days (column c). Light blue shaded regions show the 5th and 95th percentiles, and the dark blue shaded regions the 25th and 75th percentiles

.

izing the long-term average J_Q with the 28-day averaging window. Conversely, the 28-day windowed averages of J_Q at ROW and BRW improved greatly over the 7-day windows and were similar to the long-term average J_Q for all of the depths.

4 Discussion and conclusions

We observed the long-term variability of the diapycnal mixing by measuring both the diapycnal diffusivity and the vertical heat flux at four different sites that spanned over 10 degrees of latitude on the Australian NWS. In general, the winter period had more substantial mixing over the water column at all sites. Not just seasonal changes are important, however, as spring-neap variation, and tidal period changes can also modulate the intensity of diapycnal mixing. The relative influence of each of these three frequencies differed from site to site: at the BAR site only seasonal changes were important, at the LYN site both seasonal and tidal changes were important, while at the ROW and BRW sites all three of the dominant forcing frequencies were important.

The mixing showed a strong dependence on the background density stratification. We observed large seasonal variations in the diapycnal diffusivity, especially at sites and depths where the summer and winter stratification varied greatly. The seasonal variability of diffusivity was thus large in the upper water column, but smaller nearer the sea-bed where changes in stratification were small. As the vertical heat flux was less sensitive to the changes in background stratification, it is more useful for characterizing variation in the diapycnal mixing in shelf seas with their greatly varying seasonal stratification.

https://doi.org/10.5194/egusphere-2026-2498
Preprint. Discussion started: 13 May 2026

The exact relationship between low-frequency forcing processes and the induced diapycnal mixing is complex. Characterizations based simply on local shelf slope, background stratification and barotropic tidal forcing alone, for example, neglect other phenomena that can influence mixing, such as locally and remotely generated internal waves (Gong et al., 2021), frontal dynamics and transient wind forcing (e.g. tropical cyclones), for example. While the barotropic tide itself generates no vertical velocity shear in the water column, except for near the bottom boundary, it can generate and modulate propagating internal waves, in turn contributing to low-frequency spatial modulation of diapycnal mixing.

Our findings highlight the importance of low-frequency processes in determining the temporal and spatial variability of mixing in shelf seas. By not resolving low-frequency processes , there will be inaccuracies in estimating the diapycnal mixing The low-frequency processes that control the variability of diapycnal mixing are site-specific, and this has implications for the design of field sampling programs and their interpretation in terms of overall shelf mixing. For example, at the BAR site where variability in mixing was predominantly seasonal, it may be sufficient to characterize the mixing using two relatively short deployments on the order of a week long in both summer and winter. Other sites where mixing was a function of a variety of forcing (i.e., tidal phase, spring-neap and seasonal variability) likely require sustained long-term observations in order to characterize the diapycnal mixing.

To our knowledge, the diapycnal mixing estimates presented here are amongst the longest semi-continuous time-series collected to date (Moum, 2021). The length of these records, nevertheless, remain relatively small with respect to other potentially important longer-period climatological changes. Accordingly, continuing to collect long-term mixing observations from moorings remains critical to understanding and modeling diapycnal mixing in the ocean. Despite this, we recommend that the best practice for designing a sampling program to describe the distribution of mixing at a particular location is informed a priori with the aid of models, such as the barotropic tides (Egbert and Erofeeva, 2002), or remote sensing data, such as remote internal tide directional decomposition (Gong et al., 2021). Furthermore, the same tools can be used to assess the suitability of both future and historical datasets to describe the variability of mixing, and to provide some context for what the potential implications are for short observational records.

Data availability. All of the data used for this analysis is available via the Australian Ocean Data Network and the Australian Integrated Marine Observing System.

Author contributions. CW was responsible for the conceptualization, formal analysis, investigation, methodology, software, validation, visualisation and writing. GI and NLJ were responsible for the conceptualization, funding acquisition, supervision, project administration, validation and writing. MR contributed to the methodology, software, supervision and writing.

Competing interests. Author MD Rayson is a member of the editorial board of EGU Ocean Science.

https://doi.org/10.5194/egusphere-2026-2498
Preprint. Discussion started: 13 May 2026

Acknowledgements. Data were sourced from Australia's Integrated Marine Observing System (IMOS) – IMOS is enabled by the National Collaborative Research Infrastructure Strategy (NCRIS). The authors acknowledge the Australian Institute of Marine Science (AIMS) for their efforts in maintaining the North West Shelf moorings and the quality control of the data.

https://doi.org/10.5194/egusphere-2026-2498
Preprint. Discussion started: 13 May 2026

References

Bluteau, C. E., Jones, N. L., and Ivey, G. N.: Acquiring long-term turbulence measurements from moored platforms impacted by motion, Journal of Atmospheric and Oceanic Technology, 33, 2535–2551, https://doi.org/10.1175/JTECH-D-16-0041.1, publisher: American Meteorological Society, 2016.

Cael, B. and Mashayek, A.: Log-Skew-Normality of Ocean Turbulence, Physical Review Letters, 126, 224 502, https://doi.org/10.1103/PhysRevLett.126.224502, publisher: American Physical Society, 2021.

Cimatoribus, A. A., Van Haren, H., and Gostiaux, L.: Comparison of ellison and thorpe scales from Eulerian ocean temperature observations, Journal of Geophysical Research: Oceans, 119, 7047–7065, https://doi.org/10.1002/2014JC010132, arXiv: 1402.6958 Publisher: Blackwell Publishing Ltd, 2014.

Couchman, M. M., Wynne-Cattanach, B., Alford, M. H., Caulfield, C. c. P., Kerswell, R. R., MacKinnon, J. A., and Voet, G.: Data-Driven Identification of Turbulent Oceanic Mixing From Observational Microstructure Data, Geophysical Research Letters, 48, e2021GL094 978, https://doi.org/10.1029/2021GL094978, publisher: John Wiley & Sons, Ltd ISBN: 10.1029/2021, 2021.

Egbert, G. D. and Erofeeva, S. Y.: Efficient Inverse Modeling of Barotropic Ocean Tides, Journal of Atmospheric and Oceanic Technology, 19, 183–204, https://doi.org/10.1175/1520-0426(2002)019<0183:EIMOBO>2.0.CO;2, publisher: American Meteorological Society Section: Journal of Atmospheric and Oceanic Technology, 2002.

Gong, Y., Rayson, M. D., Jones, N. L., and Ivey, G. N.: Directional decomposition of internal tides propagating from multiple generation sites, Ocean Modelling, 162, 101 801, https://doi.org/10.1016/J.OCEMOD.2021.101801, publisher: Elsevier, 2021.

Huisman, J., Pham Thi, N. N., Karl, D. M., and Sommeijer, B.: Reduced mixing generates oscillations and chaos in the oceanic deep chlorophyll maximum, Nature, 439, 322–325, https://doi.org/10.1038/nature04245, 2006.

Inall, M. E., Toberman, M., Polton, J. A., Palmer, M. R., Green, J. A., and Rippeth, T. P.: Shelf Seas Baroclinic Energy Loss: Pycnocline Mixing and Bottom Boundary Layer Dissipation, Journal of Geophysical Research: Oceans, 126, https://doi.org/10.1029/2020JC016528, publisher: John Wiley and Sons Inc, 2021.

Ivey, G. N., Winters, K. B., and Koseff, J. R.: Density stratification, turbulence, but how much mixing?, Annual Review of Fluid Mechanics, 40, 169–184, https://doi.org/10.1146/annurev.fluid.39.050905.110314, iSBN: 9780824307400, 2008.

Ivey, G. N., Bluteau, C. E., and Jones, N. L.: Quantifying Diapycnal Mixing in an Energetic Ocean, Journal of Geophysical Research: Oceans, 123, 346–357, https://doi.org/10.1002/2017JC013242, publisher: Blackwell Publishing Ltd, 2018.

Jones, N. L., Ivey, G. N., Rayson, M. D., and Kelly, S. M.: Mixing Driven by Breaking Nonlinear Internal Waves, Geophysical Research Letters, 47, https://doi.org/10.1029/2020GL089591, publisher: Blackwell Publishing Ltd, 2020.

Lewin, S. F., Kaminski, A. K., McSweeney, J. M., and Waterhouse, A. F.: Multiscale mixing variability on the inner shelf, Journal of Physical Oceanography, 55, 1735–1750, 2025.

Lomb, N. R.: Least-squares frequency analysis of unequally spaced data, Astrophysics and Space Science, 39, 447–462, https://doi.org/10.1007/BF00648343, 1976.

Luneva, M. V., Wakelin, S., Holt, J. T., Inall, M. E., Kozlov, I. E., Palmer, M. R., Toberman, M., Zubkova, E. V., and Polton, J. A.: Challenging Vertical Turbulence Mixing Schemes in a Tidally Energetic Environment: 1. 3-D Shelf-Sea Model Assessment, Journal of Geophysical Research: Oceans, 124, 6360–6387, https://doi.org/10.1029/2018JC014307, publisher: John Wiley & Sons, Ltd, 2019.

MacKinnon, J. A., Zhao, Z., Whalen, C. B., Waterhouse, A. F., Trossman, D. S., Sun, O. M., St Laurent, L. C., Simmons, H. L., Polzin, K., Pinkel, R., Pickering, A., Norton, N. J., Nash, J. D., Musgrave, R., Merchant, L. M., Melet, A. V., Mater, B., Legg, S., Large, W. G.,

https://doi.org/10.5194/egusphere-2026-2498
Preprint. Discussion started: 13 May 2026

Kunze, E., Klymak, J. M., Jochum, M., Jayne, S. R., Hallberg, R. W., Griffies, S. M., Danabasoglu, G., Chassignet, E. P., Buijsman, M. C., Bryan, F. O., Briegleb, B. P., Barna, A., Arbic, B. K., Ansong, J. K., and Alford, M. H.: Climate process team on internal wave-driven ocean mixing, Bulletin of the American Meteorological Society, 98, 2429–2454, https://doi.org/10.1175/BAMS-D-16-0030.1, publisher: American Meteorological Society, 2017.

Moum, J. N.: Variations in Ocean Mixing from Seconds to Years, Annual Review of Marine Science, 13, 201–226, https://doi.org/10.1146/annurev-marine-031920-122846, 2021.

Moum, J. N. and Rippeth, T. P.: Do observations adequately resolve the natural variability of oceanic turbulence?, Journal of Marine Systems, 77, 409–417, https://doi.org/10.1016/j.jmarsys.2008.10.013, 2009.

Percival, D. B. and Walden, A. T.: Wavelet methods for time series analysis, Cambridge University Press, ISBN 0-521-64068-7, 2000.

Portwood, G. D., Kops, S. M. d. B., Taylor, J. R., Salehipour, H., and Caulfield, C. P.: Robust identification of dynamically distinct regions in stratified turbulence, Journal of Fluid Mechanics, 807, R2, https://doi.org/10.1017/jfm.2016.617, publisher: Cambridge University Press, 2016.

Rayson, M. D., Jones, N. L., and Ivey, G. N.: Observations of large-amplitude mode-2 nonlinear internal waves on the australian north west shelf, Journal of Physical Oceanography, 49, 309–328, https://doi.org/10.1175/JPO-D-18-0097.1, publisher: American Meteorological Society, 2019.

Rayson, M. D., Jones, N. L., Ivey, G. N., and Gong, Y.: A Seasonal Harmonic Model for Internal Tide Amplitude Prediction, Journal of Geophysical Research: Oceans, 126, e2021JC017 570, https://doi.org/10.1029/2021JC017570, _eprint: https://agupubs.onlinelibrary.wiley.com/doi/pdf/10.1029/2021JC017570, 2021.

Salehipour, H. and Peltier, W. R.: Diapycnal diffusivity, turbulent Prandtl number and mixing efficiency in Boussinesq stratified turbulence, Journal of Fluid Mechanics, 775, 464–500, https://doi.org/10.1017/jfm.2015.305, publisher: Cambridge University Press, 2015.

Savelyev, I. B., Martin, P. J., Fan, Y., Savidge, D. K., Shearman, R. K., Haack, T., de Paolo, T., Terrill, E. J., and Wang, Q.: An Empirical Evaluation of Turbulence Closure Models in the Coastal Ocean, Journal of Geophysical Research: Oceans, 127, e2021JC017 588, https://doi.org/10.1029/2021JC017588, publisher: John Wiley & Sons, Ltd ISBN: 10.1029/2021, 2022.

Scargle, J. D.: Studies in astronomical time series analysis. II. Statistical aspects of spectral analysis of unevenly spaced data., The Astrophysical Journal, 263, 835–853, https://doi.org/10.1086/160554, aDS Bibcode: 1982ApJ...263..835S, 1982.

Scheifele, B., Waterman, S., and Carpenter, J. R.: Turbulence and mixing in the arctic ocean's amundsen gulf, Journal of Physical Oceanography, 51, 169–186, https://doi.org/10.1175/JPO-D-20-0057.1, publisher: American Meteorological Society, 2021.

Shroyer, E. L., Moum, J. N., and Nash, J. D.: Vertical heat flux and lateral mass transport in nonlinear internal waves, Geophysical Research Letters, 37, https://doi.org/10.1029/2010GL042715, 2010.

Taylor, J. R., de Bruyn Kops, S. M., Caulfield, C. P., and Linden, P. F.: Testing the assumptions underlying ocean mixing methodologies using direct numerical simulations, Journal of Physical Oceanography, 49, 2761–2779, https://doi.org/10.1175/JPO-D-19-0033.1, publisher: American Meteorological Society, 2019.

Warner, S. J. and Moum, J. N.: Feedback of Mixing to ENSO Phase Change, Geophysical Research Letters, 46, 13 920–13 927, https://doi.org/10.1029/2019GL085415, _eprint: https://agupubs.onlinelibrary.wiley.com/doi/pdf/10.1029/2019GL085415, 2019.

Waterhouse, A. F., Mackinnon, J. A., Nash, J. D., Alford, M. H., Kunze, E., Simmons, H. L., Polzin, K. L., Laurent, L. C., Sun, O. M., Pinkel, R., Talley, L. D., Whalen, C. B., Huussen, T. N., Carter, G. S., Fer, I., Waterman, S., Naveira Garabato, A. C., Sanford, T. B., and Lee, C. M.: Global patterns of diapycnal mixing from measurements of the turbulent dissipation rate, Journal of Physical Oceanography, 44, 1854–1872, https://doi.org/10.1175/JPO-D-13-0104.1, publisher: American Meteorological Society, 2014.

https://doi.org/10.5194/egusphere-2026-2498
Preprint. Discussion started: 13 May 2026

Whiteway, T.: Australian Bathymetry and Topography Grid, June 2009, https://doi.org/10.4225/25/53D99B6581B9A, type: dataset, 2009.

Whitwell, C. A., Jones, N. L., Ivey, G. N., Rosevear, M. G., and Rayson, M. D.: Ocean Mixing in a Shelf Sea Driven by Energetic Internal Waves, Journal of Geophysical Research: Oceans, 129, e2023JC019 704, https://onlinelibrary.wiley.com/doi/abs/10.1029/2023JC019704, publisher: John Wiley & Sons, Ltd, 2024.

Winters, K. B., Lombard, P. N., Riley, J. J., and D'Asaro, E. A.: Available potential energy and mixing in density-stratified fluids, Journal of Fluid Mechanics, 289, 115–128, https://doi.org/10.1017/S002211209500125X, 1995.

Wyatt, A. S. J., Leichter, J. J., Toth, L. T., Miyajima, T., Aronson, R. B., and Nagata, T.: Heat accumulation on coral reefs mitigated by internal waves, Nature Geoscience, 13, 28–34, https://doi.org/10.1038/s41561-019-0486-4, number: 1 Publisher: Nature Publishing Group, 2020.

Zulberti, A., Jones, N. L., and Ivey, G. N.: Observations of Enhanced Sediment Transport by Nonlinear Internal Waves, Geophysical Research Letters, 47, e2020GL088 499, https://doi.org/10.1029/2020GL088499, _eprint: https://onlinelibrary.wiley.com/doi/pdf/10.1029/2020GL088499, 2020.